


# Gravitational lensing detection of an extremely dense environment around a galaxy cluster

Mauro Sereno <sup>1,2,\*</sup>, Carlo Giocoli <sup>1,2,3</sup>, Luca Izzo <sup>4</sup>, Federico Marulli <sup>1,2,3</sup>, Alfonso Veropalumbo <sup>2,3</sup>, Stefano Ettori <sup>1,3</sup>, Lauro Moscardini <sup>1,2,3</sup>, Giovanni Covone <sup>5,6</sup>, Antonio Ferragamo<sup>7,8</sup>, Rafael Barrena <sup>7,8</sup> and Alina Streblyanska<sup>7,8</sup>

**Galaxy clusters form at the highest-density nodes of the cosmic web<sup>1,2</sup>. The clustering of dark matter halos hosting these galaxy clusters is enhanced relative to the general mass distribution, with the matter density beyond the virial region being strongly correlated to the halo mass (halo bias)<sup>3</sup>. Halo properties other than mass can further enhance the halo clustering (secondary bias)<sup>4-7</sup>. Observational campaigns have ascertained the halo bias<sup>8-10</sup>, but efforts to detect this secondary bias for massive halos have been inconclusive<sup>11-13</sup>. Here, we report the analysis of the environment bias in a sample of massive clusters, selected through the Sunyaev-Zel'dovich effect by the Planck mission<sup>14,15</sup>, focusing on the detection of the environment dark matter correlated to a single cluster, PSZ2 G099.86+58.45. The gravitational lensing signal of the outskirts is very large and can be traced up to 30 megaparsecs with a high signal-to-noise ratio (about 3.4), implying environment matter density in notable excess of the cosmological mean. Our finding reveals this system to be extremely rare in the current paradigm of structure formation and, implies that enhancing mechanisms around high-mass halos can be very effective. Future lensing surveys will probe the surroundings of single haloes, enabling the study of their formation and evolution of structure.**

Here, we measure the environment bias of a single massive cluster by detection of the weak lensing (WL) signal, which distorts the shape of the background galaxies. The correlated matter around the halo imprints a peculiar feature in the shear profile<sup>16</sup>. Mass and concentration of the halo, as well as environment bias, can be determined by fitting the shear profile up to very large distances. No proxy is needed. Even though the shear measurement around a single cluster is very challenging due to high noise, the interpretation is much more direct than for stacked samples, where the noise is reduced at the cost of averaging over heterogeneous or contaminated samples.

Sunyaev-Zel'dovich (SZ) selected galaxy clusters appear to be trustful tracers of the massive end of the cosmological halo mass function<sup>17</sup>. We study the environment bias in the PSZ2LenS sample<sup>15</sup>, which consists of the 35 galaxy clusters detected by the Planck mission<sup>14</sup> in the sky portion covered by the legacy surveys CFHTLenS (Canada-France-Hawaii Telescope Lensing Survey)<sup>18</sup> and RCSLenS (Red Cluster Sequence Lensing Survey)<sup>19</sup>. PSZ2LenS is a statistically complete and homogeneous subsample of the PSZ2 catalogue<sup>14</sup>.

It is approximately mass limited, and the main halo properties are in excellent agreement with the  $\Lambda$ CDM (cold dark matter with a cosmological constant  $\Lambda$ ) scenario of structure formation<sup>15</sup>.

The WL data quality enables us to investigate the environment bias up to very large radii. Our main target is PSZ2 G099.86+58.45, the highest redshift cluster ( $z_{cl}=0.616$ ) of the PSZ2LenS sample (Fig. 1). PSZ2 G099.86+58.45 is massive. The temperature of the intra-cluster medium is  $T_x=8.9_{-1.1}^{+2.8}$  keV, as derived from the spectroscopic analysis of XMM-Newton data. The galaxy velocity dispersion is  $\sigma_v=1,040\pm 110$  km s<sup>-1</sup>. We identify the centre with the dominant brightest cluster galaxy (BCG).

PSZ2 G099.86+58.45 is located at the centre of the CFHTLS wide3 field. The angular diameter distance to the cluster is  $D_d\approx 0.98$  Gpc h<sup>-1</sup>, where  $h=H_0/(100$  km s<sup>-1</sup> Mpc<sup>-1</sup>), which is  $\sim 80\%$  of the maximum angular diameter distance reachable in our Universe. The shear can then be investigated up to very large projected proper distances ( $R=\theta D_d$ ) from the cluster centre, in relatively small angular apertures ( $\theta$ ). The lens redshift is still such that we can measure the shape distortion of a significant number of faint sources in the background. This makes PSZ2 G099.86+58.45 an ideal target, unique in PSZ2LenS. For lower redshift clusters, the limited survey area cannot cover the full radial range.

The mass distribution around PSZ2 G099.86+58.45 is recovered with the WL analysis of the differential surface density,  $\Delta\Sigma_+$  (Fig. 2). We collect the shear signal of more than 150,000 galaxies up to  $\sim 25.1$  Mpc h<sup>-1</sup> ( $\sim 1.46^\circ$ ).

Shape distortions of galaxies in CFHTLenS are measured in the  $i$  optical band<sup>20,21</sup>; photometric redshifts are estimated exploiting observations in the  $u, g, r, i$  and  $z$  bands<sup>22,23</sup>. We select background galaxies by their colours or photometric redshifts. The effective redshift of the selected source galaxies is  $z_s\approx 0.96$ . The overall level of shear systematics due to calibration errors, fitting procedure, contamination by foreground or cluster member galaxies, photometric redshift uncertainties and intrinsic alignment is at the  $\sim 6\%$  level.

The mass distribution as inferred from WL can be compared with the galaxy density at the cluster redshift. Despite the poor angular resolution of the WL analysis, the comparison between the iso-density maps suggests that the peaks in matter and galaxy density coincide (Fig. 1).

We measure the WL signal in circular annuli (Fig. 2). All the matter along the line of sight contributes to lensing. We can identify three main agents: (1) the main lens, that is, the collapsed and

<sup>1</sup>INAF - Osservatorio di Astrofisica e Scienza dello Spazio di Bologna, Bologna, Italy. <sup>2</sup>Dipartimento di Fisica e Astronomia, Alma Mater Studiorum - Università di Bologna, Bologna, Italy. <sup>3</sup>INFN, Sezione di Bologna, Bologna, Italy. <sup>4</sup>Instituto de Astrofísica de Andalucía (IAA-CSIC), Granada, Spain.

<sup>5</sup>Dipartimento di Fisica, Università di Napoli 'Federico II', Compl. Univers. di Monte S. Angelo, Napoli, Italy. <sup>6</sup>INFN, Sezione di Napoli, Compl. Università di Monte S. Angelo, Napoli, Italy. <sup>7</sup>Instituto de Astrofísica de Canarias (IAC), Tenerife, Spain. <sup>8</sup>Universidad de La Laguna, Departamento de Astrofísica, C/ Astrofísico Francisco Sánchez s/n, Tenerife, Spain. \*e-mail: [mauro.sereno@oabo.inaf.it](mailto:mauro.sereno@oabo.inaf.it)

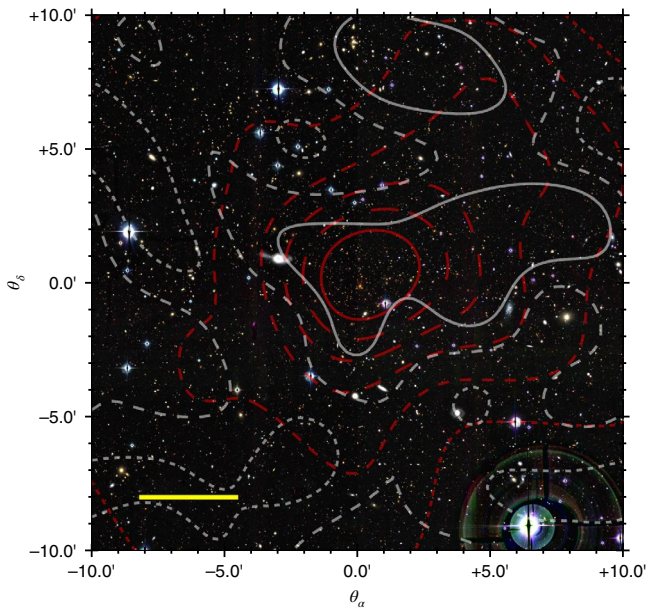


**Fig. 1 | Visible light and total mass.** Shown is the composite colour image of PSZ2 G099.86+58.45 exploiting CFHTLS *g*, *r* and *i* band images. The contours follow the mass distribution reconstructed from WL (white) and optical *i* light (red) of the galaxies with photometric redshift within  $\pm 0.06(1+z_{cl})$  of the cluster redshift ( $z_{cl}$ ). The longer the dash, the higher the contour value. The map is centred on the BCG, and north is up. Scale bar,  $1 \text{ Mpc } h^{-1}$ .

nearly virialized cluster, which is dominant at radii  $\lesssim 3 \text{ Mpc}$ ; (2) the correlated matter in the surroundings ( $\gtrsim 3 \text{ Mpc}$ ), comprised of the satellite halos, the filamentary structure and the smoothly accreting matter<sup>24,25</sup>; and (3) the uncorrelated matter from the large-scale structure (LSS), which fills the line of sight.

The measured lensing signal in the range  $10 < R < 25.1 \text{ Mpc } h^{-1}$ , where the correlated matter is the dominant term, is  $\Delta\Sigma_{+,obs} = 32.1 \pm 4.5(\text{stat.}) \pm 8.1(\text{LSS}) \pm 2.1(\text{sys.}) M_{\odot} h \text{ pc}^{-2}$ . The signal-to-noise ratio is  $\text{SNR}_{>10 \text{ Mpc}/h} \simeq 3.4$  after combining all three sources of noise. This provides a clear and model independent detection of the cluster surroundings.

The  $\Lambda\text{CDM}$  paradigm makes detailed predictions on clusters and surroundings in terms of mass and redshift of the main halo. The cluster can be modelled with a cuspy density profile<sup>26</sup> whose mass and concentration are correlated<sup>27</sup>. The density profile is truncated and the matter beyond the splashback radius is still infalling<sup>28</sup>. The correlated matter can be expressed as a two-halo term<sup>16</sup>, where the halo bias is a function of the peak height<sup>3</sup>. The LSS acts as a noise whose amplitude is determined by the effective projected power spectrum<sup>29</sup>. It is significant on very large scales.

We measure the matter distribution and compare it with  $\Lambda\text{CDM}$  predictions. The environment bias ( $b_e$ ) expresses the matter overdensity in the halo surroundings. We use two parametric modellings. First, we fit the shear profile only in the region more sensitive to the main halo ( $0.1 < R < 3 \text{ Mpc } h^{-1}$ ) with an informative prior on the mass–concentration relation<sup>27</sup> and  $b_e$  modelled as a two-halo term<sup>3</sup>. The systematic uncertainty on the theoretical halo bias is  $\sim 6\%$ , as estimated from the simulation-to-simulation scatter<sup>3</sup>, even though simulations poorly cover the mass and redshift range around PSZ2 G099.86+58.45. Within this scheme (the  $\Lambda\text{CDM}$  model), we measure mass  $M_{200} = (8.2 \pm 3.5) \times 10^{14} M_{\odot} h^{-1}$  or  $M_{500} = (5.5 \pm 2.0) \times 10^{14} M_{\odot} h^{-1}$ , concentration  $c_{200} = 3.4 \pm 0.9$  and  $b_{e,\Lambda\text{CDM}} = 11.1 \pm 2.8$ , where uncertainties include statistical and LSS noise.

The measured WL mass is in good agreement with expectations based on multi-probe proxies:  $M_{X,500} = (5.1 \pm 1.8) \times 10^{14} M_{\odot} h^{-1}$  based

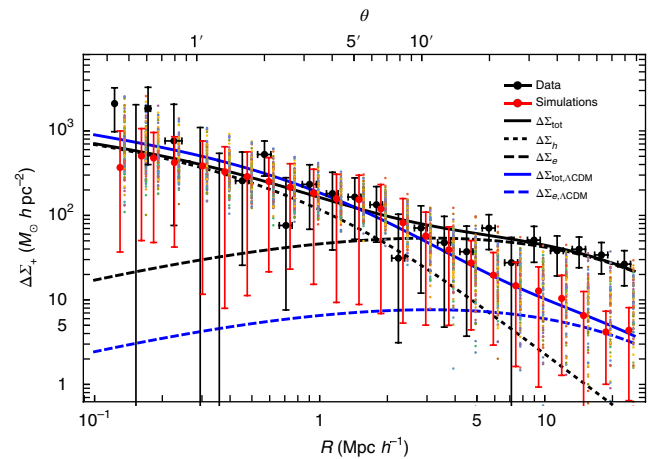


**Fig. 2 | Lensing profile.** Shown is the differential surface density ( $\Delta\Sigma_+$ ) of PSZ2 G099.86+58.45 as a function of the proper projected distance from the BCG. Black points are the measurements. The horizontal error bars are the weighted standard deviations of the distribution of radial distances in the annulus; the vertical error bars represent the square root of the diagonal elements of the total uncertainty covariance matrix, including statistical and LSS noise. Red points are the averaged simulations; small coloured points are for single realizations. The vertical red bar includes 68.3% of the simulated profiles. Red and coloured points are horizontally shifted for visualization purposes. The black line is the best fitting profile on the full radial range; the blue line plots the  $\Lambda\text{CDM}$  model. The dotted and dashed curves plot the contribution by the main halo and the correlated matter, respectively.

on  $T_X$ ;  $M_{SZ,500} = (6.1 \pm 0.8) \times 10^{14} M_{\odot} h^{-1}$  based on the integrated Compton parameter<sup>14</sup>;  $M_{\sigma,500} = (4.3 \pm 1.4) \times 10^{14} M_{\odot} h^{-1}$  based on the galaxy velocity dispersion.

Second, we fit the full profile ( $0.1 < R < 25.1 \text{ Mpc } h^{-1}$ ) with  $b_e$  as a free parameter to quantify how much the matter around the halo is overdense. We find  $b_e = 72 \pm 20$ . Priors on mass and concentration of the main halo only very marginally affect this bias estimate. The bias excess cannot be explained in terms of a severely underestimated halo mass, as confirmed by the multi-probe analysis.

The measured signal in the range  $10 < R < 25 \text{ Mpc } h^{-1}$  is much higher than the average  $\Lambda\text{CDM}$  prediction,  $\Delta\Sigma_{+,\Lambda\text{CDM}} = 5.7 \pm 1.7 M_{\odot} h \text{ pc}^{-2}$ , hinting to two possible, not mutually exclusive, causes: very overdense correlated matter boosted by formation mechanisms or projection effects from uncorrelated structure.

To quantify the degree of discrepancy, we perform numerical simulations exploiting the Lagrangian perturbation theory, where the hierarchical formation of dark matter halos is realized from an initial density perturbation field<sup>30</sup>. This method is very effective in covering the mass and redshift range we are interested in, which can be challenging for standard  $N$ -body simulations.

We derive the shear around 128 simulated halos in the redshift range  $0.54 \lesssim z \lesssim 0.71$  with average mass and redshift as PSZ2 G099.86+58.45. The signal is consistent with the analytical  $\Lambda\text{CDM}$  model (Fig. 2). The probability that an overdense line-of-sight boosts the shear at the measured level is of  $\sim 0.5\%$  considering statistical and systematic uncertainties (Fig. 3).

This is also confirmed by the analysis of the shear distortions at random locations in the CFHTLS-W3 field, where the measured signal is larger than the excess  $\Delta\Sigma_{+,obs} - \Delta\Sigma_{+,\Lambda\text{CDM}}$  with a probability of only  $\sim 0.8\%$  (Fig. 3). Most of the overdense line-of-sights are associated to PSZ2 G099.86+58.45. Considering random pointings away from the cluster ( $> 0.5 \text{ deg}$ ) and in the remaining CFHTLS fields, the probability is  $\sim 0.3\%$ , slightly underestimated with respect to the simulation-based value due to partially correlated sampling regions.

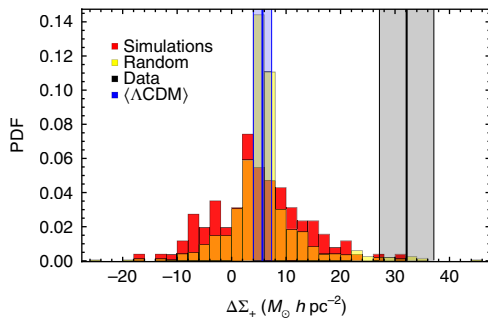


**Fig. 3 | Differential surface density of correlated matter around PS22 G099.86+58.45.** Shown is  $\Delta\Sigma_+$  in the radial range  $10 < R < 25.1 \text{ Mpc } h^{-1}$ . The histograms show the theoretical predictions, as obtained from numerical simulations (red), or as the signal at random pointings in CFHTLS-W3 added to the expected value (yellow). The black vertical line and the grey shadowed region plot the observed value for PS22 G099.86+58.45 and the 68.3% confidence region accounting for systematics and statistical uncertainties. The blue elements plot the average  $\Lambda\text{CDM}$  prediction (blue line) and the uncertainty (shadowed region).

The largest simulated lensing signals are associated to overdense regions at the lens redshift. Whereas the typical simulated system shows multiple density peaks of uncorrelated matter along the line-of-sight, the simulation with the highest signal ( $\Delta\Sigma_{+, \text{sim}} \approx 31.0 M_\odot h \text{ pc}^{-2}$ ) shows a single prominent peak at the lens redshift. Simulations strongly disfavour the uncorrelated noise as the only source of signal excess, which is related to the cluster surroundings.

The shear analysis of the environment bias of individual halos cannot be extended to the full PS22LenS sample due to e.g. incomplete area coverage or low source background density. However, the ensemble WL signal can be investigated with a stacking analysis<sup>15</sup>. The effective lensing weighted redshift of PS22LenS is  $z_{\text{stack}} = 0.20$ . We combine the shear measurements and analyse the differential density profile. As for PS22 G099.86+58.45, we fit the signal with the  $\Lambda\text{CDM}$  model in the radial range  $0.1 < R < 3.1 \text{ Mpc } h^{-1}$ , or with  $b_e$  as a free parameter for  $0.1 < R < 25.1 \text{ Mpc } h^{-1}$  (Fig. 4).

The stacked analysis probes the bias at an halo mass of  $(4.3 \pm 0.5) \times 10^{14} M_\odot h^{-1}$ . We can look for bias excess in the favourable case of high  $\text{SNR}_{>10\text{Mpc}/h} \approx 3.9$  and low LSS noise, which is now reduced by averaging over different sky regions. Even though the noise affecting the stacked sample is much smaller than for PS22 G099.86+58.45, SNRs are comparable, which further stresses the extremely high signal produced by the surroundings of PS22 G099.86+58.45. The stacked analysis cannot probe the assembly bias, since we combine the signal independently of the secondary halo properties.

The  $\Lambda\text{CDM}$  expectation for the stacked PS22LenS sample ( $b_{e, \Lambda\text{CDM}} = 5.4 \pm 0.3$ ) is compatible with the measured environment bias of the stacked clusters ( $b_e = 8.1 \pm 2.2$ ) at the 11.9% level (Fig. 4), which is statistically significant. The result does not change significantly if we consider only the subsample at low redshift and it is not driven by PS22 G099.86+58.45, which has a low lensing weight given the relatively small number of background galaxies.

The SZ selection is unique in sampling the massive end of the halo mass function and unveiling cluster properties. The environment bias for the PS22LenS sample is statistically consistent with  $\Lambda\text{CDM}$  predictions whereas the correlated matter around PS22 G099.86+58.45 lies in the extreme value tail. This is a rare case. Clustering around cluster-sized halos can be amplified for low halo concentrations, or high spins, or a significant number of subhalos with a large average distance, even though it is still uncertain why and if these different proxies of halo assembly history can exhibit different trends<sup>7</sup>. According to the statistics of peaks, the extreme

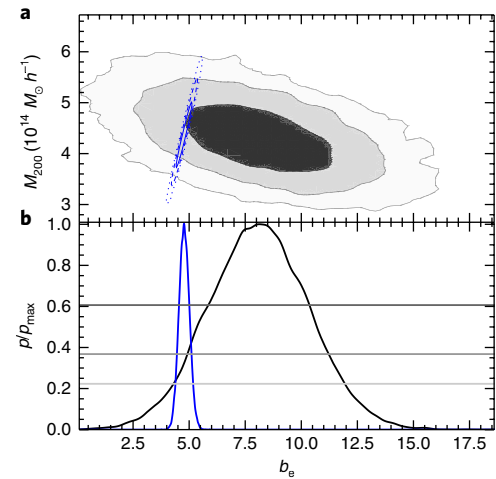


**Fig. 4 | Environment bias of PS22LenS.** Shown are the measured  $b_e$  (black lines) and the bias inferred assuming the  $\Lambda\text{CDM}$  model (blue lines). **a**, The probability distribution in the bias-mass plane. The contours include the 68.3, 95.4 and 99.7% confidence regions in two dimensions, here defined as the regions within which the probability is larger than  $e^{-2.3/2}$ ,  $e^{-6.2/2}$  or  $e^{-11.3/2}$  of the maximum, respectively. **b**, The marginalized one-dimensional distribution of the environment bias, renormalised to the maximum probability. The dark, medium and light grey horizontal lines mark the confidence limits in one dimension, that is,  $e^{-1/2}$ ,  $e^{-1}$  and  $e^{-2}$  of the maximum, respectively.

environment bias of PS22 G099.86+58.45 is associated to a peak of the primordial Gaussian density field with a very low value of the curvature  $s = |d\langle\delta\rangle/d \log M|$ , where  $\delta$  is the density fluctuation and  $M$  is the mass<sup>5</sup>. These peaks locate regions of larger background density and enhanced clustering for very massive halos. Formation and evolution mechanisms can be very effective in boosting the environment density. Next-generation galaxy surveys will routinely perform the lensing analysis of single halos out to very large radii, as we have presented here.

## Methods

**GL signal.** Our analysis exploits the public CFHTLenS and RCSLenS shear catalogues. WL data are processed with THELI<sup>20</sup> and shear measurements are obtained with lenstool<sup>21</sup>. We compute the differential projected surface density  $\Delta\Sigma_+$  in circular annuli as

$$\Delta\Sigma_+(R) = \frac{\sum_i (w_i \Sigma_{\text{cr},i}^{-2}) \epsilon_{+,i} \Sigma_{\text{cr},i}}{\sum_i (w_i \Sigma_{\text{cr},i}^{-2})} \quad (1)$$

where  $\epsilon_{+,i}$  is the tangential component of the ellipticity of the  $i$ -th source galaxy after bias correction and  $w_i$  is the weight assigned to the source ellipticity. The sum runs over the galaxies included in the annulus at transverse proper distance  $R$  from the centre, that is, the position of the brightest galaxy cluster (BCG).  $\Sigma_{\text{cr}}$  is the critical density for lensing,

$$\Sigma_{\text{cr}} = \frac{c^2}{4\pi G} \frac{D_s}{D_d D_{ds}} \quad (2)$$

where  $c$  is the speed of light in vacuum,  $G$  is the gravitational constant, and  $D_d$ ,  $D_s$  and  $D_{ds}$  are the angular diameter distances to the lens, to the source and from the lens to the source, respectively. As reference cosmological framework, we assume the concordance flat  $\Lambda\text{CDM}$  model with total matter density parameter  $\Omega_M = 0.3$ , baryonic parameter  $\Omega_b = 0.05$ , Hubble constant  $H_0 = 70 \text{ km s}^{-1} \text{ Mpc}^{-1}$ , power spectrum amplitude  $\sigma_8 = 0.8$  and initial index  $n_s = 1$ . When  $H_0$  is not specified,  $h$  is the Hubble constant in units of  $100 \text{ km s}^{-1} \text{ Mpc}^{-1}$ .

The differential surface density ( $\Delta\Sigma_+$ ) is measured between 0.1 and  $\sim 25.12 \text{ Mpc } h^{-1}$  from the cluster centre in 24 radial circular annuli equally distanced in logarithmic space. The binning is such that there are 10 bins per decade, that is, 10 bins between 0.1 and  $1 \text{ Mpc } h^{-1}$ .

The raw ellipticity components of the sources,  $e_{m,1}$  and  $e_{m,2}$ , are calibrated and corrected by applying a multiplicative and an additive correction,

$$e_i = \frac{e_{m,i} - c_i}{1 + \bar{m}} \quad (i = 1, 2) \quad (3)$$

Ellipticities of selected source are individually corrected for the estimated additive bias. The multiplicative bias  $m$  mostly depends on the measurement technique and is estimated with simulated images<sup>18,21</sup>. In each annulus, we consider the average  $\bar{m}$ , which is evaluated as<sup>31</sup>

$$\bar{m}(R) = \frac{\sum_i w_i \sum_{cr,i}^{-2} m_i}{\sum_i w_i \sum_{cr,i}^{-2}} \quad (4)$$

We identify the population of background galaxies either with a colour–colour selection<sup>32,33</sup>,

$$(g - r < 0.3) \text{ OR } (r - i > 1.3) \text{ OR } (r - i > g - r) \\ \text{AND } z_s > z_{\text{lens}} + 0.05 \quad (5)$$

or with criteria based on the photometric redshifts,

$$\text{ODDS} > 0.8 \text{ AND } z_{2.3\%} > z_{\text{lens}} + 0.05 \\ \text{AND } z_{\text{min}} < z_s < 1.2 \quad (6)$$

where the parameter ODDS quantifies the prominence of the most likely redshift<sup>22</sup> and  $z_{2.3\%}$  is the lower bound of the region including the 95.4% of the probability density distribution.  $z_{\text{min}} = 0.2$  (0.4) for the CFHTLenS (RCSLenS) fields.

The SNR of the WL detection is defined in terms of the weighted differential density  $\langle \Delta \Sigma_+ \rangle_{R_{\text{min}} < R < R_{\text{max}}}$  in the relevant radial range,

$$\text{SNR} = \frac{\langle \Delta \Sigma_+ \rangle_{R_{\text{min}} < R < R_{\text{max}}}}{\delta_+} \quad (7)$$

where  $\delta_+$  includes statistical uncertainties, systematic errors and cosmic noise added in quadrature. For our analysis of the correlated matter, we consider the signal in the radial range  $10 < R[\text{Mpc } h^{-1}] < 25.1$ .

**Lens modelling.** The differential projected surface density profile of the lens is modelled as

$$\Delta \Sigma_{\text{tot}} = \Delta \Sigma_{\text{h}} + \Delta \Sigma_{\text{e}} \pm \Delta \Sigma_{\text{LSS}} \pm \delta \Delta \Sigma_{\text{Stat}} \quad (8)$$

The term  $\Delta \Sigma_{\text{h}}$  stems from the main halo, which is described by a smoothly truncated cuspy density profile<sup>4</sup>,

$$\rho_{\text{BMO}} = \frac{\rho_s}{(r/r_s)(1+r/r_s)^2} \left( \frac{r_t^2}{r^2 + r_t^2} \right)^2, \quad (9)$$

where  $r_s$  is the scale length,  $\rho_s$  is the characteristic density and  $r_t$  is the truncation radius. We express  $r_s$  and  $\rho_s$  in terms of mass  $M_{200}$  and concentration  $c_{200}$ . The suffix 200 (500) refers to the region wherein the mean halo density is 200 (500) times the cosmological critical density at the cluster redshift. For our analysis<sup>33,35</sup>,  $r_t = 3 r_{200}$ . Details in modelling of halo truncation and outskirts do not significantly affect the shear fitting analysis at  $R \geq 10$  Mpc.

The contribution of the local environment surrounding the halo is<sup>16,35</sup>

$$\Delta \Sigma_{\text{e}}(\theta; M, z) = b_{\text{e}} \frac{\bar{\rho}_{\text{M}}(z)}{(1+z)^3 D_d^2} \int \frac{dl}{2\pi} J_2(l\theta) P_m(k_j; z) \quad (10)$$

where  $\bar{\rho}_{\text{M}}$  is the mean cosmological matter density at the cluster redshift,  $\theta$  is the angular radius,  $J_n$  is the Bessel function of  $n$ -th order and  $k_j \equiv l/[(1+z)D_d(z)]$ .  $b_{\text{e}}$  is the environment bias with respect to the linear dark matter power spectrum<sup>3,36,37</sup>,  $P_m(k_j; z)$ . We compute  $P_m$  with semi-analytical approximations<sup>38</sup>.

LSS induces a correlated noise. The cross-correlation between two angular bins  $\Delta \theta_i$  and  $\Delta \theta_j$  is<sup>29,39</sup>

$$\langle \Delta \Sigma_{\text{LSS}}(\Delta \theta_i) \Delta \Sigma_{\text{LSS}}(\Delta \theta_j) \rangle = \\ 2\pi \sum_{cr}^2 \int_0^\infty P_k(l) g(l, \Delta \theta_i) g(l, \Delta \theta_j) dl \quad (11)$$

where  $P_k(l)$  is the effective projected power spectrum of lensing. The effects of non-linear evolution on the power spectrum are accounted for with semi-analytical methods<sup>40</sup>. The function  $g$  is the filter. In an angular bin  $\theta_i < \Delta \theta < \theta_2$ ,

$$g = \frac{1}{\pi(\theta_1^2 - \theta_2^2)l} \left[ \frac{2}{l} (J_0(l\theta_2) - J_0(l\theta_1)) + \theta_j J_1(l\theta_2) - \theta_i J_1(l\theta_1) \right] \quad (12)$$

**Inference.** In a predetermined cosmological model, the lens is characterized by three parameters,  $\mathbf{p} = (M_{200}, c_{200}, b_{\text{e}})$ , which we measure with a standard Bayesian analysis<sup>41</sup>. The posterior probability density function of the parameters given the data  $\{\Delta \Sigma_+\}$  is

$$p(\mathbf{p} | \{\Delta \Sigma_+\}) \propto \mathcal{L}(\mathbf{p}) p_{\text{prior}}(\mathbf{p}) \quad (13)$$

where  $\mathcal{L}$  is the likelihood and  $p_{\text{prior}}$  represents a prior.

The likelihood is  $\mathcal{L} \propto \exp(-\chi^2)$ , where the  $\chi^2$  is written as

$$\chi^2 = \sum_{ij} [\Delta \Sigma_{+,i} - \Delta \Sigma_+(\mathbf{p})]^{-1} C_{ij}^{-1} [\Delta \Sigma_{+,j} - \Delta \Sigma_+(\mathbf{p})] \quad (14)$$

the sum extends over the radial annuli and the effective radius  $R_i$  of the  $i$ -th bin is estimated as the shear-weighted radius<sup>15</sup>.  $\Delta \Sigma_+(R_i)$  is the measured differential surface density and  $\Delta \Sigma_+(\mathbf{p}) = \Delta \Sigma_{\text{h}} + \Delta \Sigma_{\text{e}}$ .

$\Delta \Sigma_{\text{LSS}}$  and  $\delta \Delta \Sigma_{\text{Stat}}$  are treated as uncertainties. The total uncertainty covariance matrix is

$$C = C^{\text{stat}} + C^{\text{LSS}} \quad (15)$$

where  $C^{\text{stat}}$  accounts for the uncorrelated statistical uncertainties in the measured shear, whereas  $C_{ij}^{\text{LSS}} = \langle \Delta \Sigma_{\text{LSS}}(\Delta \theta_i) \Delta \Sigma_{\text{LSS}}(\Delta \theta_j) \rangle$  is due to LSS (equation (11)).

As mass prior, we consider a uniform probability distribution in the range  $0.05 \leq M_{200}/(10^{14} M_{\odot} h^{-1}) \leq 100$ , with the distribution being null otherwise.

For the concentration, we consider a lognormal distribution in the range  $1 < c_{200} < 10$ , with median value<sup>37</sup>,

$$c_{200} = A \left( \frac{1.34}{1+z} \right)^B \left( \frac{M_{200}}{8 \times 10^{14} h^{-1} M_{\odot}} \right)^C, \quad (16)$$

where  $A = 3.757$ ,  $B = 0.288$  and  $C = -0.058$ . The scatter of the mass-concentration relation is 0.25 in natural logarithms.

The prior on the bias is either a Dirac  $\delta$  function of the peak height  $\nu$ ,  $b_{\text{e}} = b_{\text{h}}[\nu(M_{200}, z)]^3$  for the  $\Lambda$ CDM model, or an uniform distribution in the range  $0.02 < b_{\text{e}} < 200$ .

**WL stacking.** We stack the lensing measurements of the PSZ2LenS clusters following a standardized approach<sup>8,9,15,33,42</sup>. The lensing signals of multiple clusters are combined in physical proper length units. The weight factor is mass-independent and the effective mass and concentration of the stacked clusters are unbiased<sup>43,44</sup>. Clusters are centred on the respective BCGs. We fit a single profile to the stacked signal to determine the ensemble properties<sup>15</sup>.

**WL systematics.** Systematic uncertainties in the shear signal are listed in Supplementary Table 1. The main errors not accounted for in equation (15) come from the calibration uncertainty of the multiplicative shear bias, the photo- $z$  accuracy and precision, and the selection of source galaxies<sup>15</sup>.

The multiplicative bias is well controlled, but a calibration uncertainty in the shape measurements can persist at the level of a few per cents. By comparison of separate shape catalogues<sup>45</sup>, the systematic uncertainty can be estimated in  $\delta m \approx 0.03$ .

Cluster members or foreground galaxies dilute the lensing signal. Our selection criteria suffer by a  $\lesssim 2\%$  contamination<sup>15</sup>.

Miscentring can underestimate the shear signal at small scales and affect the concentration measurement<sup>8</sup>. However, the effect is negligible at large scales of  $\geq 10$  Mpc.

Photometric redshift systematics can impact WL analyses by biasing the estimation of the surface critical density. As source redshifts, we consider the peak of the probability density, as applicable to well-behaved distributions. The systematic error associated to either a bias ( $\sim 4.5\%$ ) or a scatter ( $\sim 3\%$ ) in the photo- $z$  estimates is quantified for  $z_{\text{cl}} \approx 0.62$  with simulations reproducing the CFHTLenS survey<sup>15</sup>.

Improper halo modelling can affect mass and concentration estimates at a few per cent<sup>46</sup>. However, as far as the halo truncation is accounted for, the effect on  $b_{\text{e}}$  is negligible.

The role of cluster projection is marginal. Two clusters that fall along the same line of sight may be blended by the SZ cluster finder into a single, larger cluster. Whereas the Compton parameters add approximately linearly, the lensing amplitude  $\Delta \Sigma_+$  is a differential measurement and the estimated  $b_{\text{e}}$  of the blended system can be well below the sum of the two aligned halos. However, the chance to have two or more Planck clusters aligned is  $\sim 5\%$ . At  $z = 0.616$ , the systematic error is then negligible ( $< 1\%$ ).

Intrinsic galaxy alignment of nearby galaxies (II) can contaminate the signal. Furthermore, galaxies experience a shear caused by the foreground tidal gravitational field. If the foreground galaxy has an intrinsic ellipticity that is linearly correlated with this field, shape and shear are correlated (GI). In the

intrinsic alignment model<sup>47,48</sup>, the power spectra of intrinsic alignment II and GI are proportional to the matter power spectrum,

$$P_{II} = F_z^2 P_\delta, \quad P_{GI} = F_z^2 P_\delta \quad (17)$$

with

$$F_z = -C_{\rho_{Cr}}(z=0) \frac{\Omega_M}{D(z)} \quad (18)$$

where  $D(z)$  is the linear growth factor normalized to unity today and  $C_{\rho_{Cr}} = 5 \times 10^{-14} h^{-2} M_\odot^{-1} \text{Mpc}^3$ . At  $z=0.616$ , the combined systematic error from II and GI is negligible ( $<1\%$ ).

The total level of systematic uncertainties is  $\sim 6.5\%$ .

**WL stress tests.** We check for potential residual sources of errors in the WL analysis of PSZ2 G099.86+58.45. Not properly corrected systematics can affect the cross-component of the shear. We verify that it is consistent with zero as expected (Supplementary Fig. 1). The  $P$  value of the null hypothesis is 0.08.

We repeat the analysis of the tangential component under different assumptions to check whether the systematic level is sufficiently smaller than the statistical noise; see Supplementary Table 2.

The cluster catalogue and the shape measurements are taken from different data sets. The distribution of lenses is then uncorrelated with systematics in shape measurements<sup>49</sup>.

Residual errors can be significant if the PSF (point spread function) is very anisotropic. We can consider only fields that pass the CFHTLenS WL selection (WL pass)—fields with a low level of PSF anisotropy contamination as estimated from the analysis of the star-galaxy cross-correlation<sup>18,20</sup>. The result agrees with the reference case, as also confirmed by the analysis performed disregarding the additive bias correction, that is, by putting  $c_2 = 0$ .

To check if the excess can be associated to a single structure nearby or in projection, we measure the shear in sectors. The signals in the northwest, northeast, southeast and southwest quadrants are compatible with the signal in the full field of view, whereas the bias exceeds the average  $\Lambda$ CDM prediction in each sector. This confirms that the excess is not related to foreground or background massive halos.

The selection of background galaxies is checked by comparing results obtained using either the colour-colour (equation (5)) or the photo- $z$  method (equation (6)).

The effects of centring or cluster member dilution are checked by considering the SZ centroid as lens centre or excising the inner region at  $R < 0.5 \text{Mpc} h^{-1}$ .

The extent of errors affecting the photo- $z$  estimates is checked either adding a positive bias  $+0.01(1+z)$  to the peak of the redshift distributions of the galaxies in the field or randomly scattering the peaks with a Gaussian distribution with standard deviation  $\sigma_z = 0.04(1+z)$ .

Variations in the shear signal due to the cosmological model are negligible too, as checked by considering the cosmological parameters from the nine-year Wilkinson Microwave Anisotropy Probe (WMAP9) observations<sup>50</sup>.

The halo bias is defined with respect to the linear power spectrum. However, even considering non-linearities (NL- $P_\delta$ ), the estimated bias is still much larger than the average  $\Lambda$ CDM prediction.

The above tests confirm that systematics are negligible.

**Random pointings.** General features from the LSS can be studied by extracting the signal around random points with the same procedure used for the cluster analysis. We measure the differential density associated to 1,000 random positions in the CFHT-W3 field at redshift  $z=0.616$  and we stack the signals. Both the tangential and the cross-component of the shear are consistent with a null signal (Supplementary Fig. 2). The  $P$  value of the null hypothesis is 0.30 (0.12) for the tangential (cross) component. This further confirms that the main systematics have been eliminated and that the signal excess around PSZ2 G099.86+58.45 is significant (Fig. 3).

Residual systematics can affect the stacking analysis due to incomplete annuli for clusters near the border of the field of view or at low redshift, and to partially overlapping regions for nearby clusters. We compute the stacked signal for 100 PSZ2LenS-like catalogues of 35 random sources reproducing the input redshift distribution and the field locations. Both the tangential and the cross-component of the stacked shear are consistent with a null signal (Supplementary Fig. 3). The  $P$  value of the null hypothesis is 0.49 (0.25) for the tangential (cross) component.

**Numerical simulations of the WL signal.** We generate the WL signal around clusters using a sample of self-consistent halo model simulations. We produce a set of halo catalogues within past light cone simulations up to  $z=1$  using Pinocchio<sup>50</sup>. Pinocchio is a fast code to generate catalogues of cosmological dark matter halos starting from an initial power spectrum and perturbing it using the Lagrangian perturbation theory (LPT) model. For this work, we perform the Pinocchio simulations using the 3LPT approximation<sup>51</sup>. The large-scale matter density distribution in halos accurately reproduces the results of  $N$ -body simulations.

Out of 512 light-cone realizations, we extract a sample of 128 halos with mass and redshift similar to PSZ2 G099.86+58.45. We construct the effective convergence map of the full light cone of the main cluster plus correlated and uncorrelated systems up to redshift  $z=1$  (Supplementary Fig. 4), using the MOKA<sup>52</sup> and the WL-MOKA<sup>53</sup> tools. In particular, we resimulate the main halo using MOKA, which generates triaxial systems populated with dark matter substructures mimicking halos from numerical simulations. We place a BCG, which is modelled using a Jaffe profile, in the centre of the cluster. The halo dark matter distribution is adiabatically contracted as consequence. Correlated matter and uncorrelated LSS are modelled as isolated NFW (Navarro-Frenk-White)<sup>56</sup> halos with a mass-concentration relation consistent with field halos<sup>57</sup>. The aperture of our field of view is  $3^\circ$  by side; by construction our light cones are pyramids, where the observer is located at the vertex and the base is at a fixed source redshift,  $z=1$ . We compute the shear field from the convergence maps using fast Fourier methods.

We finally measure the reduced shear profile around the cluster centre assuming a large source density of 32 galaxies arcminute<sup>-2</sup> to make it sure that the measured signal is due to real features in the simulated matter distribution. It is not due to measurement uncertainties.

Alternatively to the shear signal, the cluster environment is studied by analysing the mass distribution as a function of redshift. We measure the total matter collapsed in halos (except for the central cluster) above the minimum threshold of  $7 \times 10^{11} M_\odot h^{-1}$ . The redshift slices are  $\Delta z = 0.05$  thick and we consider only halos in limited angular radial apertures ranging from  $0.15^\circ$  to  $1.5^\circ$ . In Supplementary Fig. 5, we plot the result of an aperture of  $1^\circ$ . The mass is rescaled by the lensing distance kernel  $D_{\text{lens}} = D_{\text{ds}}/D_s$ .

**X-ray analysis.** The X-ray analysis is performed on archival XMM-Newton data observed on 8 November 2013. We apply the standard calibration to obtain the event lists for the EPIC detector, using the cifbuild, odfinger and emchain packages<sup>54</sup>. Background sources are excluded with the cheese tool. We preliminarily apply a standard filtering with the mos-filter and pn-filter package for the MOS and PN detector, respectively, to check the contamination by soft-proton background. The high number of CCDs (three) in the anomalous mode for the MOS1 detector leads us to consider only the MOS2 and the PN detectors for our analysis. The particle background model for our starting images and spectra is produced with the mos\_back and pn\_back packages.

We select the time intervals less contaminated by the soft-proton background. Using images in the soft and hard XMM bands, we identify and remove extra X-ray sources located in the region of interest. Finally, we obtain the spectral files for the source, the background and the instrumental responses.

The spectral analysis is performed with XSPEC<sup>55</sup>. We consider an absorbed APEC thermal model for the cluster component, with metal abundance fixed at  $Z = 0.3 Z_\odot$ .

We take into account different background sources: (1) an unabsorbed thermal component representing the local hot bubble<sup>56</sup>; (2) an absorbed thermal component that models the intergalactic medium and the cool halo<sup>56</sup>; and (3) an absorbed power-law with spectral index  $\alpha = 1.46$  representing the unresolved background of cosmological sources<sup>57</sup>. In addition, we included emission lines rising from the solar wind charge exchange at 0.56 and 0.65 keV. We finally include three Gaussian models to consider bright fluorescent lines at 1.49, 1.75 and 8 keV, due to the  $K\alpha$  of the Al, Si and Cu, respectively.

The spectra are finally fitted in the range 0.4–7.2 keV. The X-ray temperature is converted in mass exploiting calibrated scaling relations<sup>58</sup>.

**Optical spectroscopy.** The spectroscopic redshift analysis is performed under an International time project (ITP13-08) at the Canary Islands observatories<sup>59</sup>. We preliminarily calculate the photometric redshift of the cluster using archival Sloan Digital Sky Survey (SDSS) DR12 data<sup>60</sup>. Candidate cluster members show coherent colours in agreement with  $z_{\text{phot}} = 0.63 \pm 0.03$ .

To confirm the cluster and obtain an estimate of the galaxy velocity dispersion, we perform spectroscopic observations using the OSIRIS spectrograph of the 10.4 m GTC telescope at Roque de los Muchachos Observatory in the Canary Islands during March 2014. We obtain spectroscopic redshifts for eight galaxy members by setting the long-slit in two position angles. The exposure time is 3 ks for each position. The full wavelength range, 4,000–9,000 Å, is covered with a resolution of  $R \approx 500$ .

The spectroscopic data reduction is performed with IRAF tasks<sup>61</sup>; radial velocities are obtained using XCSAO, that is, the cross-correlation technique<sup>62</sup> implemented in the IRAF task RVS AO, with six spectrum templates of E, S0, Sa, Sb, Sc and Irr galaxies<sup>63</sup>.

We measure radial velocities for eight cluster members, including the BCG at RA = 213.696611°, DEC = 54.784321° (J2000) and  $z_{\text{BCG}} = 0.6139 \pm 0.0002$ . We also consider four redshifts from SDSS-DR12 and 32 redshifts from literature<sup>64</sup>, for a total of 44 unique galaxy members. Radial velocities are homogenized by correcting for the mean difference of five repeated spectra.

All galaxy members are placed within 2.5 Mpc from the cluster centre and their velocities are within  $\pm 2,500 \text{ km s}^{-1}$  from the BCG. The full spectroscopic dataset reveals that PSZ2 G099.86+58.45 is at  $z_{\text{spec}} = 0.616 \pm 0.002$ .

The galaxy velocity dispersion  $\sigma_v = 1,044 \pm 113 \text{ km s}^{-1}$  is estimated with the gapper scale estimator<sup>65</sup> and aperture correction<sup>66</sup>. This estimate can be used as a mass proxy through a scaling relation<sup>67</sup>.

**Data availability.** The data that support the plots within this paper and other findings of this study are available from the corresponding author upon reasonable request. Material is also publicly available at <http://pico.oabo.inaf.it/sereno/>. The WL data are obtained with MegaPrime/MegaCam, a joint project of CFHT and CEA/IRFU, at the Canada–France–Hawaii Telescope (CFHT), which is operated by the National Research Council (NRC) of Canada, the Institut National des Sciences de l'Univers of the Centre National de la Recherche Scientifique (CNRS) of France, and the University of Hawaii. The CFHTLenS and RCSLenS catalogues, including photometry and lensing shape information, are publicly available at <http://www.cadc-ccda.hia-ihp.nrc-cnrc.gc.ca/en/community/cfhtlens/query.html> and <http://www.cadc-ccda.hia-ihp.nrc-cnrc.gc.ca/en/community/rcslens/query.html>, respectively.

Received: 2 November 2017; Accepted: 1 June 2018;

Published online: 9 July 2018

## References

- Kaiser, N. On the spatial correlations of Abell clusters. *Astrophys. J.* **284**, L9–L12 (1984).
- Sheth, R. K. & Tormen, G. On the environmental dependence of halo formation. *Mon. Not. R. Astron. Soc.* **350**, 1385–1390 (2004).
- Tinker, J. L. et al. The large-scale bias of dark matter halos: numerical calibration and model tests. *Astrophys. J.* **724**, 878–886 (2010).
- Wechsler, R. H., Zentner, A. R., Bullock, J. S., Kravtsov, A. V. & Allgood, B. The dependence of halo clustering on halo formation history, concentration, and occupation. *Astrophys. J.* **652**, 71–84 (2006).
- Dalal, N., White, M., Bond, J. R. & Shirokov, A. Halo assembly bias in hierarchical structure formation. *Astrophys. J.* **687**, 12–21 (2008).
- Li, Y., Mo, H. J. & Gao, L. On halo formation times and assembly bias. *Mon. Not. R. Astron. Soc.* **389**, 1419–1426 (2008).
- Mao, Y.-Y., Zentner, A. R. & Wechsler, R. H. Beyond assembly bias: exploring secondary halo biases for cluster-size haloes. *Mon. Not. R. Astron. Soc.* **474**, 5143–5157 (2018).
- Johnston, D. E. et al. Cross-correlation weak lensing of SDSS galaxy clusters II: cluster density profiles and the mass–richness relation. Preprint at <https://arxiv.org/abs/0709.1159> (2007).
- Sereno, M. et al. New constraints on  $\sigma_8$  from a joint analysis of stacked gravitational lensing and clustering of galaxy clusters. *Mon. Not. R. Astron. Soc.* **449**, 4147–4161 (2015).
- Dvornik, A. et al. A KiDS weak lensing analysis of assembly bias in GAMA galaxy groups. *Mon. Not. R. Astron. Soc.* **468**, 3251–3265 (2017).
- More, S. et al. Detection of the splashback radius and halo assembly bias of massive galaxy clusters. *Astrophys. J.* **825**, 39 (2016).
- Zu, Y., Mandelbaum, R., Simet, M., Rozo, E. & Rykoff, E. S. On the level of cluster assembly bias in SDSS. *Mon. Not. R. Astron. Soc.* **470**, 551–560 (2017).
- Busch, P. & White, S. D. M. Assembly bias and splashback in galaxy clusters. *Mon. Not. R. Astron. Soc.* **470**, 4767–4781 (2017).
- Planck Collaboration et al. Planck2015 results. XXVII. The second Planck catalogue of Sunyaev–Zeldovich sources. *Astron. Astrophys.* **594**, A27 (2016).
- Sereno, M. et al. PSZ2LenS. Weak lensing analysis of the Planck clusters in the CFHTLenS and in the RCSLenS. *Mon. Not. R. Astron. Soc.* **472**, 1946–1971 (2017).
- Oguri, M. & Takada, M. Combining cluster observables and stacked weak lensing to probe dark energy: self-calibration of systematic uncertainties. *Phys. Rev. D* **83**, 023008 (2011).
- Rossetti, M. et al. Measuring the dynamical state of Planck SZ-selected clusters: X-ray peak - BCG offset. *Mon. Not. R. Astron. Soc.* **457**, 4515–4524 (2016).
- Heymans, C. et al. CFHTLenS: the Canada–France–Hawaii Telescope Lensing Survey. *Mon. Not. R. Astron. Soc.* **427**, 146–166 (2012).
- Hildebrandt, H. et al. RCSLenS: the Red Cluster Sequence Lensing Survey. *Mon. Not. R. Astron. Soc.* **463**, 635–654 (2016).
- Erben, T. et al. CFHTLenS: the Canada–France–Hawaii Telescope Lensing Survey—imaging data and catalogue products. *Mon. Not. R. Astron. Soc.* **433**, 2545–2563 (2013).
- Miller, L. et al. Bayesian galaxy shape measurement for weak lensing surveys — III. Application to the Canada–France–Hawaii Telescope Lensing Survey. *Mon. Not. R. Astron. Soc.* **429**, 2858–2880 (2013).
- Hildebrandt, H. et al. CFHTLenS: improving the quality of photometric redshifts with precision photometry. *Mon. Not. R. Astron. Soc.* **421**, 2355–2367 (2012).
- Benjamin, J. et al. CFHTLenS tomographic weak lensing: quantifying accurate redshift distributions. *Mon. Not. R. Astron. Soc.* **431**, 1547–1564 (2013).
- Colberg, J. M., Krughoff, K. S. & Connolly, A. J. Intercluster filaments in a  $\Lambda$  CDM Universe. *Mon. Not. R. Astron. Soc.* **359**, 272–282 (2005).
- Eckert, D. et al. Warm-hot baryons comprise 5–10 per cent of filaments in the cosmic web. *Nature* **528**, 105–107 (2015).
- Navarro, J. F., Frenk, C. S. & White, S. D. M. The structure of cold dark matter halos. *Astrophys. J.* **462**, 563–575 (1996).
- Meneghetti, M. et al. The MUSIC of CLASH: predictions on the concentration-mass relation. *Astrophys. J.* **797**, 34 (2014).
- Diemer, B., Mansfield, P., Kravtsov, A. V. & More, S. The splashback radius of halos from particle dynamics. II. Dependence on mass, accretion rate, redshift, and cosmology. *Astrophys. J.* **843**, 140 (2017).
- Schneider, P., van Waerbeke, L., Jain, B. & Kruse, G. A new measure for cosmic shear. *Mon. Not. R. Astron. Soc.* **296**, 873–892 (1998).
- Monaco, P. et al. An accurate tool for the fast generation of dark matter halo catalogues. *Mon. Not. R. Astron. Soc.* **433**, 2389–2402 (2013).
- Viola, M. et al. Dark matter halo properties of GAMA galaxy groups from 100 square degrees of KiDS weak lensing data. *Mon. Not. R. Astron. Soc.* **452**, 3529–3550 (2015).
- Oguri, M. et al. Combined strong and weak lensing analysis of 28 clusters from the Sloan Giant Arcs Survey. *Mon. Not. R. Astron. Soc.* **420**, 3213–3239 (2012).
- Covone, G., Sereno, M., Kilbinger, M. & Cardone, V. F. Measurement of the halo bias from stacked shear profiles of galaxy clusters. *Astrophys. J. Lett.* **784**, L25 (2014).
- Baltz, E. A., Marshall, P. & Oguri, M. Analytic models of plausible gravitational lens potentials. *J. Cosmol. Astropart. Phys.* **1**, 15 (2009).
- Oguri, M. & Hamana, T. Detailed cluster lensing profiles at large radii and the impact on cluster weak lensing studies. *Mon. Not. R. Astron. Soc.* **414**, 1851–1861 (2011).
- Sheth, R. K. & Tormen, G. Large-scale bias and the peak background split. *Mon. Not. R. Astron. Soc.* **308**, 119–126 (1999).
- Bhattacharya, S., Habib, S., Heitmann, K. & Vikhlinin, A. Dark matter halo profiles of massive clusters: theory versus observations. *Astrophys. J.* **766**, 32 (2013).
- Eisenstein, D. J. & Hu, W. Power spectra for cold dark matter and its variants. *Astrophys. J.* **511**, 5–15 (1999).
- Hoekstra, H. How well can we determine cluster mass profiles from weak lensing? *Mon. Not. R. Astron. Soc.* **339**, 1155–1162 (2003).
- Smith, R. E. et al. Stable clustering, the halo model and non-linear cosmological power spectra. *Mon. Not. R. Astron. Soc.* **341**, 1311–1332 (2003).
- Sereno, M., Giocoli, C., Ettori, S. & Moscardini, L. The mass-concentration relation in lensing clusters: the role of statistical biases and selection effects. *Mon. Not. R. Astron. Soc.* **449**, 2024–2039 (2015).
- Mandelbaum, R., Seljak, U. & Hirata, C. M. A halo mass-concentration relation from weak lensing. *J. Cosmol. Astropart. Phys.* **8**, 006 (2008).
- Okabe, N., Smith, G. P., Umetsu, K., Takada, M. & Futamase, T. LoCuSS: the mass density profile of massive galaxy clusters at  $z=0.2$ . *Astrophys. J.* **769**, L35 (2013).
- Umetsu, K. et al. CLASH: weak-lensing shear-and-magnification analysis of 20 galaxy clusters. *Astrophys. J.* **795**, 163 (2014).
- Jarvis, M. et al. The DES science verification weak lensing shear catalogues. *Mon. Not. R. Astron. Soc.* **460**, 2245–2281 (2016).
- Sereno, M., Fedeli, C. & Moscardini, L. Comparison of weak lensing by NFW and Einasto halos and systematic errors. *J. Cosmol. Astropart. Phys.* **1**, 042 (2016).
- Bridle, S. & King, L. Dark energy constraints from cosmic shear power spectra: impact of intrinsic alignments on photometric redshift requirements. *New J. Phys.* **9**, 444 (2007).
- Heymans, C. et al. CFHTLenS tomographic weak lensing cosmological parameter constraints: mitigating the impact of intrinsic galaxy alignments. *Mon. Not. R. Astron. Soc.* **432**, 2433–2453 (2013).
- Miyatake, H. et al. The weak lensing signal and the clustering of BOSS galaxies. I. Measurements. *Astrophys. J.* **806**, 1 (2015).
- Hinshaw, G. et al. Nine-year Wilkinson Microwave Anisotropy Probe (WMAP) observations: cosmological parameter results. *Astrophys. J. Suppl. Ser.* **208**, 19 (2013).
- Munari, E. et al. Improving fast generation of halo catalogues with higher order Lagrangian perturbation theory. *Mon. Not. R. Astron. Soc.* **465**, 4658–4677 (2017).
- Giocoli, C., Meneghetti, M., Bartelmann, M., Moscardini, L. & Boldrin, M. MOKA: a new tool for strong lensing studies. *Mon. Not. R. Astron. Soc.* **421**, 3343–3355 (2012).
- Giocoli, C. et al. Fast weak-lensing simulations with halo model. *Mon. Not. R. Astron. Soc.* **470**, 3574–3590 (2017).
- Snowden, S. L., Mushotzky, R. F., Kuntz, K. D. & Davis, D. S. A catalog of galaxy clusters observed by XMM-Newton. *Astron. Astrophys.* **478**, 615–658 (2008).
- Arnau, K. A. in *Astron. Soc. Pacific Conf. Proc.* Vol. 101 *Astronomical Data Analysis Software and Systems V* (eds Jacoby, G. H. & Barnes, J.) 17 (ASP, 1996).

56. Kuntz, K. D. & Snowden, S. L. The X-ray-emitting components toward  $\ell = 111^\circ$ : the local hot bubble and beyond. *Astrophys. J.* **674**, 209–219 (2008).
57. Takey, A., Schwobe, A. & Lamer, G. The 2XMMi/SDSS galaxy cluster survey. I. The first cluster sample and X-ray luminosity–temperature relation. *Astron. Astrophys.* **534**, A120 (2011).
58. Vikhlinin, A. et al. Chandra cluster cosmology project. II. Samples and X-ray data reduction. *Astrophys. J.* **692**, 1033–1059 (2009).
59. Planck Collaboration. Planck intermediate results. XXXVI. Optical identification and redshifts of Planck SZ sources with telescopes at the Canary Islands observatories. *Astron. Astrophys.* **586**, A139 (2016).
60. Alam, S. et al. The eleventh and twelfth data releases of the Sloan Digital Sky Survey: final data from SDSS-III. *Astrophys. J. Suppl. Ser.* **219**, 12 (2015).
61. Tody, D. in *Proc. SPIE Vol. 627: Instrumentation in Astronomy VI* (ed. Crawford, D. L.) 733 (SPIE, 1986).
62. Tonry, J. & Davis, M. A survey of galaxy redshifts. I — Data reduction techniques. *Astron. J.* **84**, 1511–1525 (1979).
63. Kennicutt, R. C. Jr. A spectrophotometric atlas of galaxies. *Astrophys. J. Suppl. Ser.* **79**, 255–284 (1992).
64. McGreer, I. D. et al. A bright lensed galaxy at  $z = 5.4$  with strong Ly $\alpha$  emission. Preprint at <https://arxiv.org/abs/1706.09428> (2017).
65. Beers, T. C., Flynn, K. & Gebhardt, K. Measures of location and scale for velocities in clusters of galaxies — a robust approach. *Astron. J.* **100**, 32–46 (1990).
66. Sifón, C. et al. The Atacama Cosmology Telescope: dynamical masses for 44 SZ-selected galaxy clusters over 755 square degrees. *Mon. Not. R. Astron. Soc.* **461**, 248–270 (2016).
67. Evrard, A. E. et al. Virial scaling of massive dark matter halos: why clusters prefer a high normalization cosmology. *Astrophys. J.* **672**, 122–137 (2008).

### Acknowledgements

We thank J. A. R. Martín for coordinating the spectroscopic campaign and L. D'Avino for suggestions on the rendering of Fig. 1. S.E. and M.S. acknowledge financial support from contracts ASI-INAF I/009/10/0, NARO15 ASI-INAF I/037/12/0, ASI 2015-046-R.0 and ASI-INAF n.2017-14-H.0. C.G. acknowledges support from the Italian Ministry

for Education, University, and Research (MIUR) through the SIR individual grant SIMCODE, project number RBSI14P4IH, and the Italian Ministry of Foreign Affairs and International Cooperation, Directorate General for Country Promotion for Country Promotion. L.I. acknowledges support from the Spanish research project AYA 2014-58381-P. L.M. acknowledges support from the grants ASI n.I/023/12/0 and PRIN MIUR 2015. A.F., A.S. and R.B. acknowledge financial support from the Spanish Ministry of Economy and Competitiveness (MINECO) under AYA 2014-60438-P, ESP2013-48362-C2-1-P and the 2011 Severo Ochoa Program MINECO SEV-2011-0187 projects. This article includes observations made with the Gran Telescopio Canarias (GTC) operated by Instituto de Astrofísica de Canarias (IAC) with telescope time awarded by the CCI International Time Programme at the Canary Islands observatories (programme ITP13-8). The simulations were run on the Marconi supercomputer at Cineca thanks to the projects IsC10\_MOKAlen3 and IsC49\_CIBra01.

### Author contributions

All authors contributed to the interpretation and presentation of the results. M.S.: lead author; project concept, planning, and design; writing; lensing, statistical, and cosmological analyses. C.G.: numerical simulations. L.I.: X-ray analysis. F.M. and A.V.: cosmological analysis. S.E. and L.M.: planning and interpretation. G.C.: cluster sample selection. A.F., A.S. and R.B.: galaxy kinematics.

### Competing interests

The authors declare no competing interests.

### Additional information

**Supplementary information** is available for this paper at <https://doi.org/10.1038/s41550-018-0508-y>.

**Reprints and permissions information** is available at [www.nature.com/reprints](http://www.nature.com/reprints).

**Correspondence and requests for materials** should be addressed to M.S.

**Publisher's note:** Springer Nature remains neutral with regard to jurisdictional claims in published maps and institutional affiliations.